

Theoretical modeling and experimental study of Japanese “Watari-ago” joints

Keita Ogawa¹ · Yasutoshi Sasaki¹ · Mariko Yamasaki¹

Received: 21 November 2014 / Accepted: 29 June 2015 / Published online: 19 July 2015
© The Japan Wood Research Society 2015

Abstract Timber joints used in traditional Japanese constructions have no metal plates or fasteners. Because these joints resist external force by embedment to each member, they show high ductility. The ductile joints get much attention recently. Japanese “Watari-ago” joint used in horizontal structure is one such ductile joint. The joint consists of two beams with interlocking notches, which build resistance against in-plane shear forces. In this paper, the mechanical behavior of “Watari-ago” joints is studied experimentally and theoretically. Experimental results show that “Watari-ago” joints can retain resistance after reaching their yield strength and that mechanical behavior varies depending upon notch shape and size. In theoretical research, a predicting model of mechanical behavior of the joint is developed by applying wooden embedment theory. The model proposed in this study also identifies the size that gives optimal mechanical performance. By numerical calculation on the basis of the model, the authors find it quantitatively that the increase of the sizes of beam width and notch depth has greatly effect on the moment resistance.

Keywords Timber joint · Mechanical modeling · Moment–deformation angle relationship · Wooden embedment

Introduction

Traditional Japanese timber constructions are the result of a long progress in the art of timber construction. Despite exposure to earthquakes and typhoons, these constructions persist to the present day. Because the constructions consist mainly of columns and beams, the mechanical behavior of the joints is important in evaluating their mechanical performance under external forces. The joints used in these constructions consist of wood-to-wood without metal plates or fasteners. These joints resist external force by embedment to each member. Under embedment forces, wood may be loaded far over its elastic limit. Thus, the joints depending on wooden embedment property for the resistance also have high ductility.

Ductile joints get much attention recently. These joints have high energy absorption capacity, and they are expected to delay or avoid their brittle failure. Many researchers have tried to develop new ductile joints [1–4]. The ductility can also be found in traditional timber joints. Japanese “Nuki” joints [5, 6], slot-plug type joint seen in China [7], Taiwanese “Nuki” joint [8, 9] and dovetail joint used in Korea [10–12] has been already studied mechanically.

Japanese “Watari-ago” joint is one such timber joint used in a floor or a horizontal roof member of traditional Japanese timber constructions, as shown in Fig. 1. When horizontal forces due to earthquakes or winds act on the structure, the “Watari-ago” joint resist the in-plane shear forces. “Watari-ago” joints consist of two notched beams, as shown in Fig. 2. The interlocking of these notches resists the applied load. Although there has been experimental study of the mechanical behavior of “Watari-ago” joints [13], few theoretical studies have been conducted. Because the joint has complex design, three-dimensional deformation under the embedment force is required for the theoretical analysis. It is

✉ Yasutoshi Sasaki
ysasaki@nagoya-u.jp

¹ Department of Biosphere Resources Science, Graduate School of Bioagricultural Sciences, Nagoya University, Nagoya 464-8601, Japan

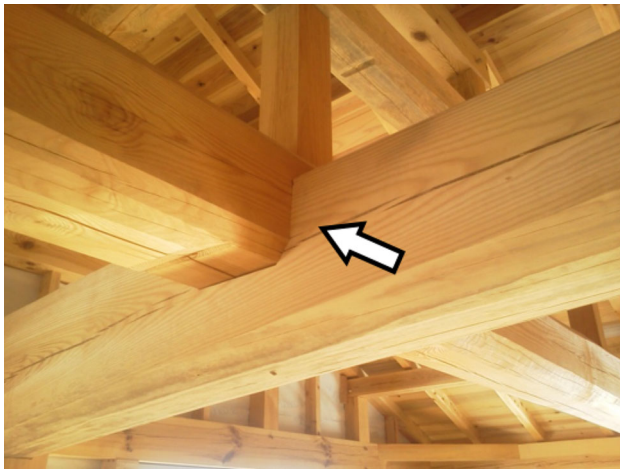


Fig. 1 A “Watari-ago” joint in horizontal roof members, consisting of two notched beams

a reason that the analysis of “Watari-ago” joint becomes more difficult than other joints.

This paper attempts to develop a calculation method for predicting the mechanical behavior of the “Watari-ago” joint based on wooden embedment properties, and discuss the relationship between size and mechanical behavior based on our theory.

Theory

Formulation of displacement under embedment loading

Embedment occurs at the contact area of interlocking notches when an in-plane shear force acts on the joint. “Watari-ago” joint seems to produce its resistance by the

embedment. The purpose of this study is to apply an embedment theory to a formulation of the mechanical behavior of the joint.

Under an embedment loading, a deformation is also found at an indirectly loaded area, as illustrated in Fig. 3. The surface deformation at the area is generally expressed with an exponential curve like Eq. (1) [14].

$$Z = \delta \times \exp(-\alpha X) \tag{1}$$

Inayama made a theory with this equation, describing an embedment property of wood [14]. The theory describes the material properties in the elastic region well. However, it does not cover plastic deformation. To describe the mechanical behavior of the “Watari-ago” joint after yield deformation, this study expands the theory to represent the wooden embedment properties in the plastic region.

The exponential curve expressed by Eq. (1) starts from the edge of the steel plate as shown in Fig. 3. At determining an end point of the exponential curve, a decay point is set [14]. The decay point is assumed that displacement is essentially zero. The point is positioned at the distance between the edge of steel plate and the end point of an exponential curve as shown in Fig. 3. The distance was then called decay length and is assumed to be $1.5Z'$, where Z' is thickness of wood member [15]. The shape of the exponential curve is determined by a coefficient α . In the indirectly loaded area, the volume deformation $v_{X=1.5Z'}$ in the range of decay length ($0 \leq X \leq 1.5Z'$) is assumed to be 0.9 times the original volume deformation $v_{X \rightarrow \infty}$ ($0 \leq X$). It is explained by Eq. (2) [14]:

$$\frac{v_{X=1.5Z'}}{v_{X \rightarrow \infty}} = 1 - \exp(-1.5Z'\alpha) \approx 0.9 \tag{2}$$

From Eq. (2), coefficient used in the exponential curve α is derived as $1.5/Z'$. The coordination of the decay point is

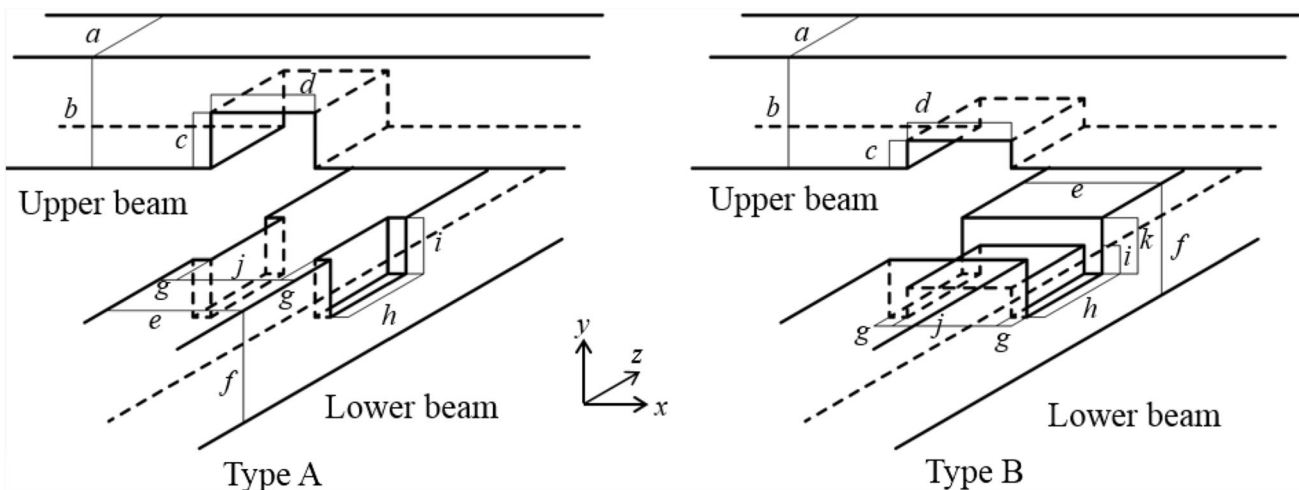
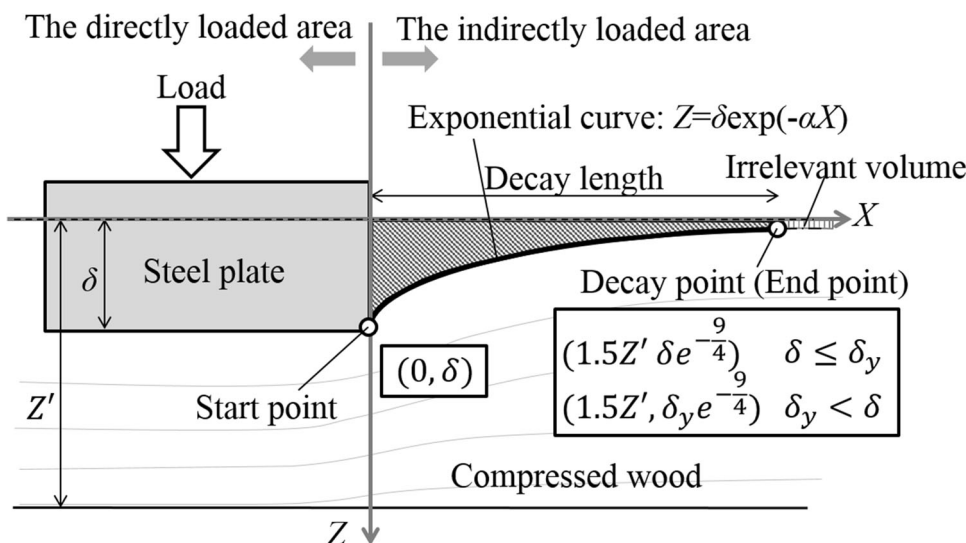


Fig. 2 Design of two types of “Watari-ago” joint. *a–d* Size parameters in upper beam. *e–k* Size parameters in lower beam. Pairs of size parameters (*a* and *h*, *c* and *i*, *d* and *j*) have same value because of geometrical relationship

Fig. 3 Surface shape of indirectly loaded area under embedment loading, taken a side view of small clear wood specimen. An embedment deformation is divided on the boundary of the Z axis. The left side is called the directly loaded area, and right side the indirectly loaded area in this research. The surface shape of the indirectly loaded area is expressed as an exponential curve



then derived by assigning $X = 1.5Z'$ to Eq. (1). It becomes $(1.5Z', \delta e^{-9/4})$.

Inayama assumed the fixed value of α as $1.5/Z'$ [14]. However, for large displacement, it is undesirable to continue using the embedment displacement δ for the coordinate of the decay point. The reason for this is that the irrelevant volume becomes larger because the displacement at the decay point is increasing due to an increase in δ . The coefficient α then was divided in this research when the deformation becomes large. In the case of large displacement, the coordinate of decay point is fixed at the case that the displacement δ reaches the yield displacement δ_y . The coordinate is expressed as $(1.5Z', \delta_y e^{-9/4})$. The authors then derive another formula of α in the range of $\delta_y < \delta$. The coefficient α in the range is derived by assigning the coordinate $(1.5Z', \delta_y e^{-9/4})$ to Eq. (1). Therefore, the coefficient α used in this study is obtained as

$$\alpha = \begin{cases} \frac{3}{2Z'} & (\delta \leq \delta_y) \\ \frac{3}{2Z'} - \frac{2}{3Z'} \log \frac{\delta_y}{\delta} & (\delta_y < \delta) \end{cases} \quad (3)$$

Formulation of mechanical behavior of “Watari-ago” joint

The derivation of the theoretical model for predicting the mechanical behavior of the “Watari-ago” joint is described in this section. Three assumptions are made for the derivation:

Assumption 1 When in-plane shear force acts on the specimen, embedment deformation is found at the contact area perpendicular to the grain, as shown in Fig. 4a.

Assumption 2 When the deepest part of a contact area reaches yield displacement δ_y , plastic deformation occurs

partially, as shown in Fig. 4b. The embedment force is calculated based on Hooke’s law in the elastic deformation region. For plastic deformation, the embedment force is calculated by multiplying a reduction coefficient r to describe non-linear behavior. The reduction coefficient r is defined as the ratio between the slopes of the plastic and elastic deformation regions on a stress–strain diagram of wooden embedment. In this research, the value of r is obtained from embedment test with small clear specimen as described later.

Assumption 3 If there are gaps at contact areas of the joint (as shown in Fig. 5), the structure cannot produce its resistance at initial loading until the notches start interlocking by additional loading.

Based on these assumptions, the moment resistance M produced in the “Watari-ago” joint can be calculated by the following equations. The derivation in this study starts from Hook’s low, which simply express a stress–strain relationship. By multiplying size parameters to the strain in the low, the embedment forces P_u and P_l produced in upper or lower beam shown in Fig. 4a are given as

$$P_u = \frac{V_u}{a} E_{90}, \quad P_l = \frac{V_l}{j} E_{90} \quad (4)$$

where P_u and P_l are the respective embedment forces produced on the upper and lower beams, V_u and V_l are the volume deformations on the upper and lower beams (expressed by the darker parts in Fig. 4a), and E_{90} is the modulus of elasticity perpendicular to grain. The variables a and j are the sizes of the notch (see Fig. 2). According to Eq. (4), the embedment forces P_u and P_l depend on the volume deformations V_u and V_l . Calculations of V_u and V_l are thus important for predicting moment resistance M .

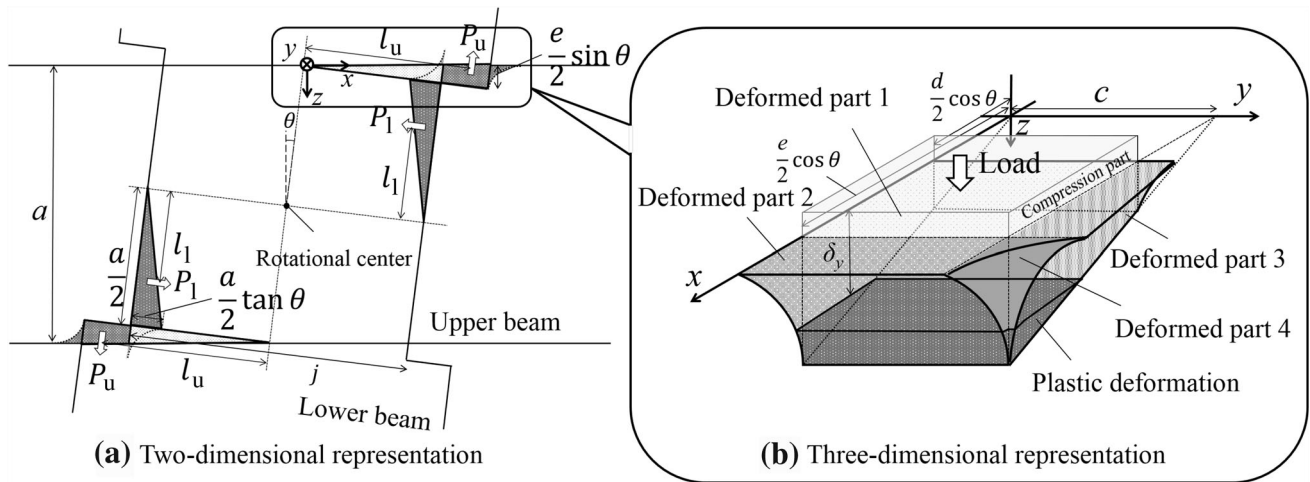
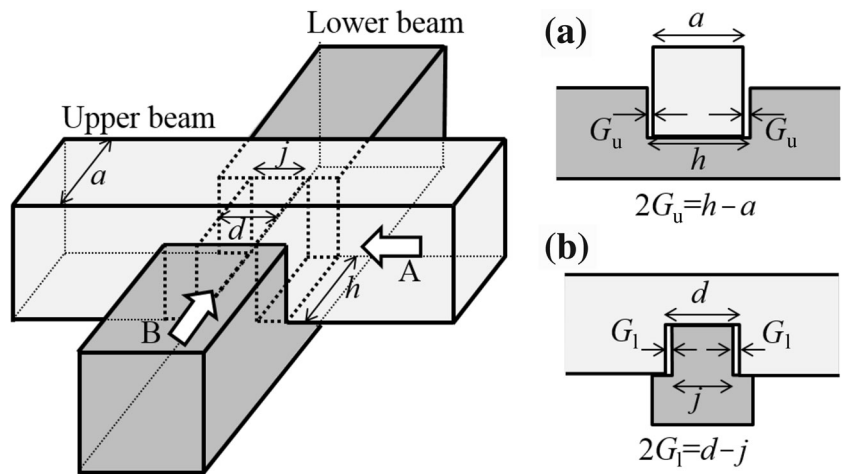


Fig. 4 **a** Geometry of compressed deformation of “Watari-ago” joint under a deformation angle θ (top view of the joint in Fig. 2). Darker parts mean deformed areas. **b** Three dimensionally expression of a deformed part in upper beam. It is divided into 4 parts. The axis x, y, z is according to Fig. 2. a, d, e and j size parameters in Fig. 2, P_u and P_l embedment forces produced on the upper and lower beams, l_u and l_l length from the rotational center to loading points P_u and P_l

z is according to Fig. 2. a, d, e and j size parameters in Fig. 2, P_u and P_l embedment forces produced on the upper and lower beams, l_u and l_l length from the rotational center to loading points P_u and P_l

Fig. 5 Gaps at the contact area. G_u gap seen from the viewing point A. G_l gap seen from the viewing point B



For the calculation of volume deformation, contact areas are divided into four smaller components by the following process (see Fig. 4b).

Deformed part 1 Deformation at directly forced area. Volume deformation at this part is named V_{x1} .

Deformed part 2 Deformation at an indirectly loaded area, adjacent to deformed part 1, and parallel to the grain. Volume deformation at this part is named V_{x2} .

Deformed part 3 Deformation at an indirectly loaded area, adjacent to deformed part 1, and perpendicular to the grain. Volume deformation at this part is named V_{x3} .

Deformed part 4 Deformation at an indirectly loaded area, and adjacent to the deformed parts 2 and 3. Volume deformation at this part is named V_{x4} .

The index x is substituted for u or l in the case of the upper and lower beams, respectively.

The deformation volume V_u describes the total volume deformation at a contact area on the upper beam. It can be written as

$$V_u = V_{u1} + V_{u2} + V_{u3} + V_{u4} \tag{5}$$

The volume deformation of the deformed part 1 V_{u1} is expressed in Fig. 6a including plastic area. Thus, we can geometrically derive it:

$$\begin{aligned} V_{u1} &= \frac{1}{2}c \left(\frac{d}{2} \sin \theta + \frac{e}{2} \sin \theta \right) \left(\frac{d}{2} \cos \theta - \frac{e}{2} \cos \theta \right) \\ &= \frac{1}{8}c(e^2 - d^2) \sin \theta \cos \theta \end{aligned} \tag{6}$$

Volume deformations V_{u2} and V_{u3} in Fig. 6a, b are then found by integration of exponential curves describing the

surface shapes of the indirectly loaded area. These volume deformations can be written as

$$V_{u2} = c \int_0^{\frac{3a}{2}} \frac{e}{2} \sin \theta \times \exp(-\alpha x) dx \tag{7}$$

$$V_{u3} = \int_{\frac{d}{2} \cos \theta}^{\frac{e}{2} \cos \theta} \int_0^{\frac{3a}{2n}} x \tan \theta \times \exp(-any) dy dx \tag{8}$$

where the coefficient n in Eq. (8) represents the grain direction [14]. This will be described later; the value of the coefficient n is 5. For the calculation of volume deformation V_{u4} , we assume the exponential curve in the y direction start from the exponential curve at the edge of deformed part 2, as shown in Fig. 6b. The volume deformation then becomes

$$V_{u4} = \int_0^{\frac{3a}{2}} \int_0^{\frac{3a}{2n}} \frac{e}{2} \sin \theta \times \exp(-\alpha x) \times \exp(-any) dy dx \tag{9}$$

When the deformation angle θ is larger than the yield deformation angle θ_y , the deformation volume V_u is divided into elastic volume deformation V_{ue} and plastic volume deformation V_{up} (shown in darker shading in Figs. 4b and 6). As shown in Fig. 4b, the overall volume deformation V_u can be divided into the elastic volume deformation V_{uei} and plastic volume deformation V_{upi} . The index i is substituted with 1–4 according to the deformation parts described earlier. The overall volume deformation then becomes

$$V_u = \sum_{i=1}^4 V_{ui} = \sum_{i=1}^4 (V_{uei} + V_{upi}) \tag{10}$$

The yield deformation angle θ_y is defined as the angle for which the largest displacement $(e \sin \theta)/2$ reaches yield displacement δ_y . The yield displacement δ_y is considered

as a function of the sizes, the coefficient α and allowable stress for long sustained embedment loading f_m [16]:

$$\delta_y = \frac{2.4 \alpha f_m}{E_{90} \sqrt{C_x C_y C_{xm} C_{ym}}} \tag{11}$$

where

$$C_x = 1 + \frac{1}{\alpha e} \left(1 - \exp\left(-\frac{3a}{2} \alpha\right) \right),$$

$$C_y = 1 + \frac{1}{\alpha n c} \left(1 - \exp\left(-\frac{3a}{2} \alpha n\right) \right)$$

$$C_{xm} = 1 + \frac{4}{\alpha e}, C_{ym} = 1 + \frac{4}{\alpha n c}$$

The authors now derive the plastic volume deformations V_{up1} in Eq. (10). As shown in Figs. 4b and 6, the plastic volume deformation V_{up1} at part 1 are calculated using the length l_{p1} of the top surface of the plastically deformed in deformation part 1. Geometrically, we obtain

$$l_{p1} = \frac{e}{2} \cos \theta - \frac{\delta_y}{\tan \theta} \tag{12}$$

The plastic volume deformation at part 1, V_{up1} , is described with l_{p1} :

$$V_{up1} = \begin{cases} \frac{c}{2} l_{p1} \left(\frac{e}{2} \sin \theta - \delta_y \right) & \left(\frac{d}{2} \sin \theta \leq \delta_y \right) \\ \frac{c}{2} \left(\frac{e}{2} \sin \theta + \frac{d}{2} \sin \theta - 2\delta_y \right) \left(\frac{e}{2} - \frac{d}{2} \right) \cos \theta & \left(\frac{d}{2} \sin \theta \geq \delta_y \right) \end{cases} \tag{13}$$

For the deformed part 2, the length l_{p2} of the top surface of the plastically deformed in deformed part 2 (Fig. 6a) is obtained by substituting the yield displacement δ_y for the z in exponential curve (Eq. (1)):

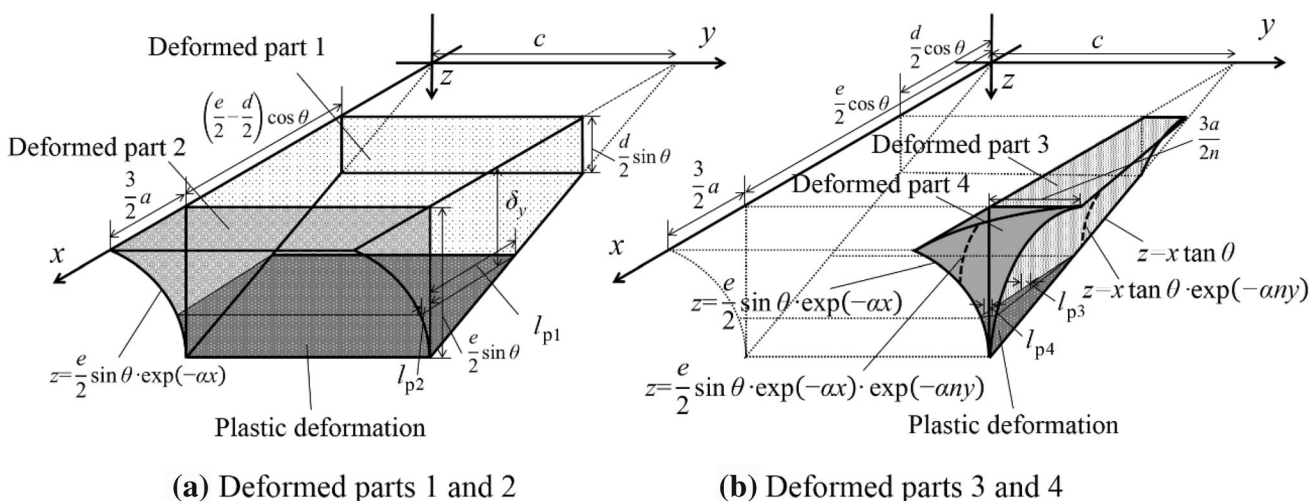


Fig. 6 Size parameters and equations that make up the deformed parts (detailed view of Fig. 4b). l_{p1} , l_{p2} , l_{p3} and l_{p4} length of the top surface of the plastically deformation in deformed part 1–4

$$l_{p2} = -\frac{1}{\alpha} \log \frac{2\delta_y}{e \sin \theta} \tag{14}$$

The plastic volume deformation at part 2, V_{up2} , can be expressed as

$$V_{up2} = c \int_0^{l_{p2}} \left(\frac{e}{2} \sin \theta \times \exp(-\alpha x) - \delta_y \right) dx \tag{15}$$

The length l_{p3} of the top surface of the plastic deformation in deformed part 3 (Fig. 6b) and the plastic volume deformation at part 3, V_{up3} , is given by forms similar to Eqs. (14) and (15),

$$l_{p3} = -\frac{1}{\alpha n} \log \frac{\delta_y}{x \tan \theta} \tag{16}$$

$$V_{up3} = \begin{cases} \int_{\frac{e}{2} \cos \theta - l_{p1}}^{\frac{e}{2} \cos \theta} \int_0^{l_{p3}} (x \tan \theta \times \exp(-\alpha ny) - \delta_y) dy dx & \left(\frac{d}{2} \sin \theta \leq \delta_y \right) \\ \int_{\frac{e}{2} \cos \theta}^{\frac{e}{2} \cos \theta + l_{p1}} \int_0^{l_{p3}} (x \tan \theta \times \exp(-\alpha ny) - \delta_y) dy dx & \left(\frac{d}{2} \sin \theta \geq \delta_y \right) \end{cases} \tag{17}$$

The volume deformations V_{up4} is also calculated by the similar way:

$$l_{p4} = -\frac{1}{\alpha n} \log \frac{2\delta_y}{e \sin \theta \times \exp(-\alpha x)} \tag{18}$$

$$V_{up4} = \int_0^{l_{p2}} \int_0^{l_{p4}} \left\{ \frac{e}{2} \sin \theta \times \exp(-\alpha x) \times \exp(-\alpha ny) - \delta_y \right\} dy dx \tag{19}$$

Expressed in Eq. (10), the volume deformations V_{ui} is the sum of the elastic volume deformation V_{uei} and plastic volume deformation V_{upi} . Therefore,

$$V_{uei} = V_{ui} - V_{upi} \tag{20}$$

The moment resistance M_u on the upper beam produced due to embedment is given as follows, using the embedment forces in Eq. (4), the length l_u from the rotational center to the loading point and the reduction coefficient r written in above,

$$M_u = \left(\frac{E_{90}}{a} \sum_{i=1}^4 V_{uei} + r \frac{E_{90}}{a} \sum_{i=1}^4 V_{upi} \right) l_u \times 2 \tag{21}$$

Then the length l_u is simply assumed as $e/3$ to avoid the derivation become complexity although the length l_u should be changed when considering the indirectly forced area and yielding.

It is possible that the volume deformations in lower beam V_{lei} and V_{lpi} is calculated by the similar Eqs. (4–21). Therefore, the moment resistance on the lower beam M_l is calculated as

$$M_l = \left(\frac{E_{90}}{j} \sum_{i=1}^4 V_{lei} + r \frac{E_{90}}{j} \sum_{i=1}^4 V_{lpi} \right) l_l \times 2 \tag{22}$$

The total moment resistance produced in the “Watari-ago” joint, M , is expressed as

$$M = M_u + M_l \tag{23}$$

If gaps described in the Assumption 3 exist in the real structure, moment resistances M_u or M_l are not produced until the notches start interlocking by additional loading. The assumption can be expressed by considering angular lags θ_u and θ_l . The moments M_u or M_l cannot be produced until the deformation angle reached θ_u or θ_l , respectively. By defining the gaps G_u and G_l as in Fig. 5, these lags θ_u and θ_l in the deformation angles are expressed as

$$\theta_u = \frac{2G_u}{e} = \frac{h-a}{e}, \theta_l = \frac{2G_l}{a} = \frac{j-d}{a} \tag{24}$$

Materials and methods

Full-scale test specimens

Thirty full-scale specimens were tested for experimental analysis of the mechanical behavior of “Watari-ago” joint. These were cross specimens of Japanese cedar (*Cryptomeria japonica* D.DON) with an interlocking “Watari-ago” joint at their center. The overall size was 1500 × 1500 mm. Two types of notch shape were used for the lower beams. These are shown in Fig. 2 as Type A and Type B. Six different series of notch dimensions were used; these are shown in Table 1, where the size parameters a, b, \dots, k and the gap sizes G_u and G_l are as described in Figs. 2 and 5. The values in the table are desired values; therefore, there are slight errors in actual specimens. The parameters enclosed in parentheses (h, i and j) have the same value with the next parameters because of the geometrical relationship. Five specimens were produced for each series.

Loading method

The experimental setup is shown in Fig. 7. A steel-framed fatigue testing machine was used for the test. The top of the specimen was connected with pins to a hydraulic actuator, while the remaining three edges were connected to the steel frame. In-plane shear forces were applied to the top of the specimen with reverse cyclic loading. The loading sequence consisted of nine cyclic steps with three identical cycles, as shown in Fig. 8. The deformation angle amplitudes θ of each of the cyclic steps were $\pm 1/450, 1/300, 1/200, 1/150, 1/100, 1/75, 1/50, 1/30,$ and $1/7$ rad (at the maximum stroke of the machine).

Stroke speed was 200 mm/min. For measuring the load P and deformation angle θ , a load cell and two displacement gages were used. These were recorded simultaneously with a dynamic data logger at a sampling frequency of 5 Hz.

Results and discussion

Test results of full-scale specimens

Similar failure modes were found in most full-scale specimens. Embedment failure occurred in all of the contact areas, as shown in Fig. 9a. It is clear that the behavior of the “Watari-ago” joint depends on embedment properties. Series II and IV specimens showed a distinct failure not observed in other specimens. Shear failures starting from the corner of the notch are seen at large deformation angles; this is seen in Fig. 9b.

Figure 10 shows the hysteresis characteristics of the “Watari-ago” joints. The moment was calculated by multiplying the load by the length between the pins at the top and bottom specimen edges. The deformation angle θ was obtained by using the distance H between the two displacement gages and their measured values v_1 and v_2 :

$$\theta \approx \tan \theta = \frac{v_1 - v_2}{H} \tag{25}$$

As the deformation angle becomes large, the “Watari-ago” joints produce greater moment resistance. Even if the deformation angle greatly exceeded the yield deformation angle, the moment resistance kept increasing; it is clear that “Watari-ago” joints have high ductility. At the second or third loading instance of the cyclic steps described in the previous section, the stiffness decrease was not obvious for small deformation angles (below approximately 0.03 rad). However, once the deformation angle increased over 0.1 rad, the specimen showed little moment resistance at the second or third loading. This is attributed to residual strain at contact areas.

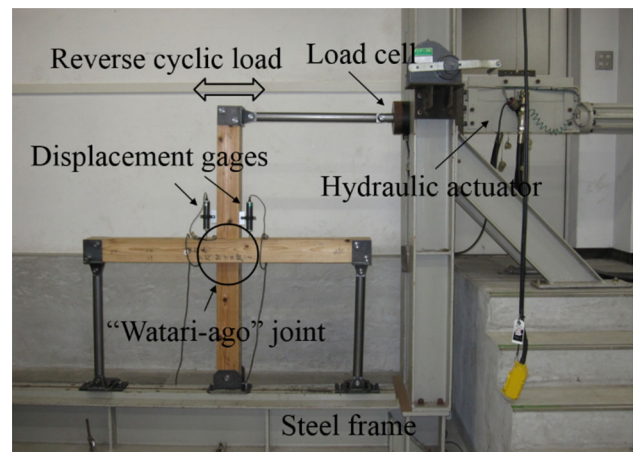


Fig. 7 Experimental setup

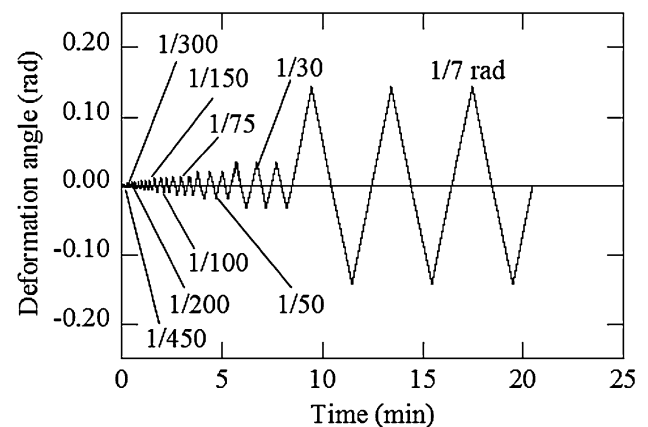


Fig. 8 Loading sequence

The hysteresis characteristics are different between each series according to differences in notch size and shape. Series III specimens showed little initial resistance due to the existence of gaps at the contact area, but large moment resistance occurred after contacting. Series IV specimens showed little moment resistance at the initial loading like series III; however, it did not show large stiffness after

Table 1 Sizes of “Watari-ago” joint specimens

Series	Type	a (h) (mm)	b (mm)	c (i) (mm)	d (j) (mm)	e (mm)	f (mm)	g (mm)	k (mm)	G_u (mm)	G_l (mm)
I	A	120	150	60	90	120	180	15	–	0.00	0.00
II	A	120	150	60	72	120	180	24	–	0.06	0.00
III	A	150	120	60	90	120	180	15	–	0.68	0.00
IV	A	120	180	60	120	150	120	15	–	0.97	0.76
V	B	120	180	30	120	150	120	15	60	0.44	0.00
VI	B	120	150	30	90	120	180	15	60	0.00	0.00

The parameters a, b, \dots, k refer Fig. 2

The gap sizes G_u and G_l refer Fig. 5

The values were desired values, and therefore there were errors in actual specimens

The parameters enclosed in parentheses (h, i, j) have the same value with the next parameters because of the geometrical relationship

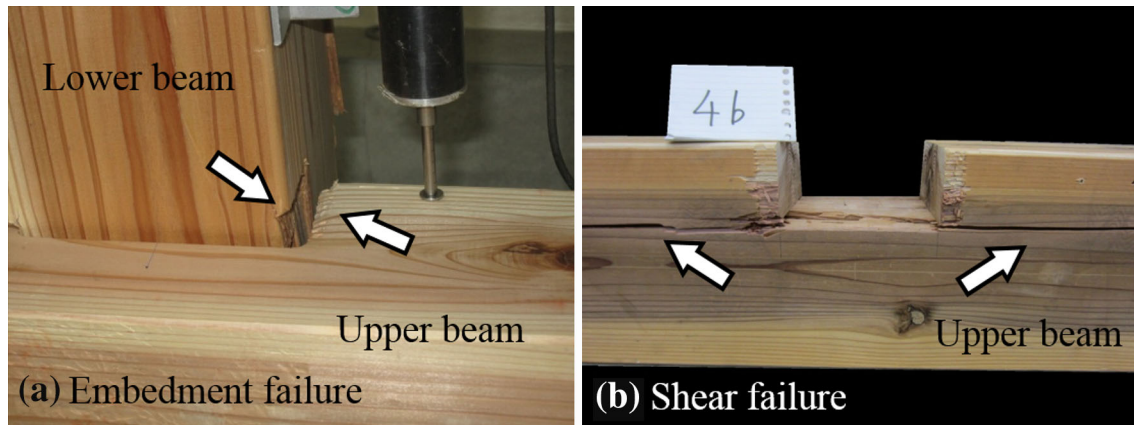


Fig. 9 Failure mode

contacting. When shear failure occurred as in Fig. 9b, Series IV specimens showed an abrupt decrease in moment resistance. Thus, shear failure at large deformation angles is an important factor for decrement of moment resistance. Series VI specimens showed less stiffness than others.

The bilinear (perfect elasto-plastic) model for evaluating mechanical characteristics based on energy analysis, which is generally used for mechanical research of wooden structural components in Japan [17], is applied in this study. The thin lines in Fig. 11 and Table 2 are the results of this applying; the thin lines are envelope curves which are made by taking the largest moment in each deformation angle as shown in Fig. 10 and the mechanical characteristics show average values. Series III and V specimens, which have large beam width, show larger maximum

moment resistance M_{\max} , moment at yield point M_y and ultimate moment M_u than other specimens. The moment resistances at $1/120$ rad, $M_{1/120}$, of series III is small. These specimens have large gaps at contact areas. Thus, the existence of gaps is an important factor contributing to the hysteresis characteristics, especially at initial loading.

Theoretical results

Figure 11 also shows comparisons of theoretical and experimental results. Thick lines represent the theoretical results while thin lines represent the experimental ones. The parameters used in the theoretical predictions are as follows. Size parameters a , b , c , ..., k are described in Fig. 2 and Table 1. According to the reference [14], E_{90} is

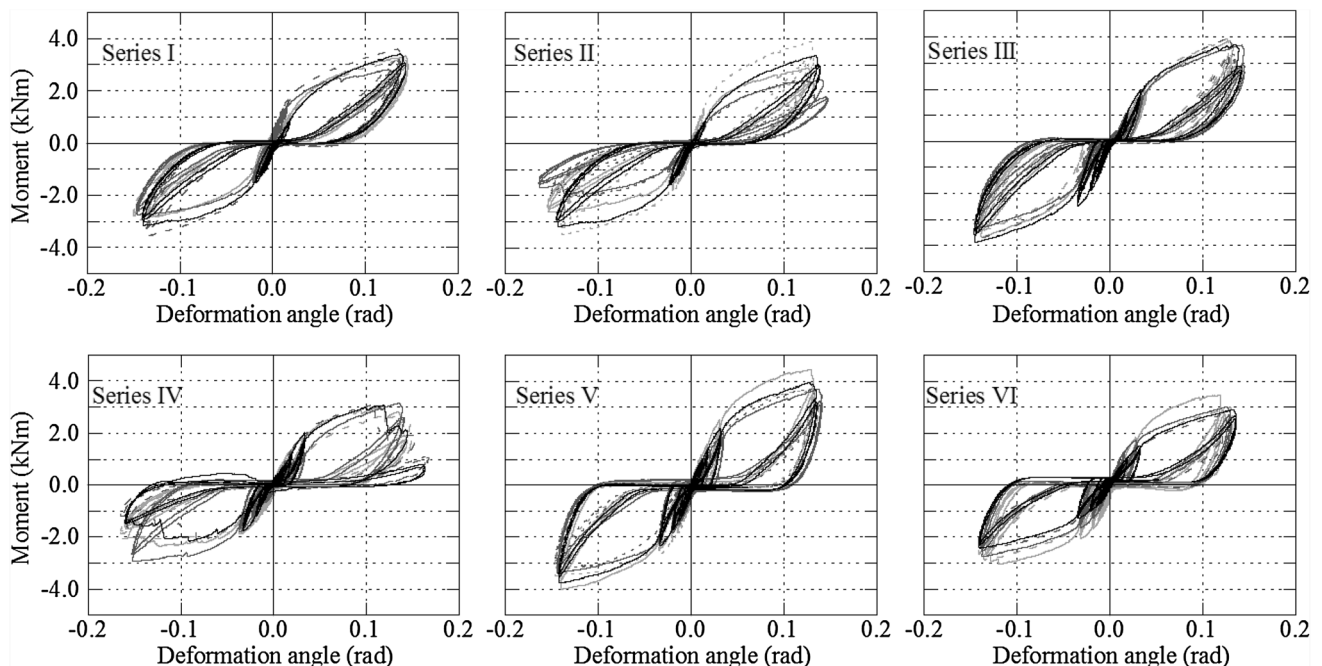


Fig. 10 Hysteresis characteristics of the “Watari-ago” joints. Series I to VI refer Table 1

assumed by multiplying E_0 by 1/50, where E_0 is the modulus of elasticity in compression parallel to the grain. E_0 is 7.6 GPa, as obtained by a standard compression test according to JIS Z 2101 [18], performed separately. The reduction coefficient r was found to be 0.065 from the stress–strain diagrams obtained by the additional embedment experiment according to JIS Z 2101 [18]. The values of the gaps are shown in Table 1. The allowable stress for long sustained embedment loading f_m is 1.96 MPa [19]. The coefficient n representing the grain direction is 5 [14].

The theoretical results reflect accurately the experimental results, as shown in Fig. 11. It has opened up the possibility of theoretical simulation of the mechanical behavior of the joint. However, the accuracy of rotational stiffness is not sufficient in most series. The possible reasons and future issues of it are raised: (1) The modulus of elasticity E_0 was got from the small clear specimens, while in contrast, the contact areas of the actual joint specimens had different conditions from them such as incline of annual ring and insufficient processing of surface. The consistency verification of the parameters (e.g., modulus of elasticity E_0) is one of the future issues. (2) The length l_u was assumed to a fixed value as $e/3$; however, l_u should be changed due to the existence of the indirectly loaded area and yielding. (3) The friction forces should be produced in actual joints, and the friction should be taken into consideration in the future study. It should be noted that the little moment resistance during initial loading, especially shown in series III and IV specimens, can be predicted by considering the existence of contact gaps.

Relationship between notch size and mechanical behavior

It is clear that notch size is a significant factor for the mechanical behavior of the “Watari-ago” joint. In this research, the mechanical behaviors of fictitious joints are calculated by the theoretical method discussed in previous section “theory” for elucidating a mechanically efficient design of “Watari-ago” joint. The notch sizes of “Watari-ago” joints are freely changed according to several cases described below and illustrated in Fig. 12.

Case 1 Length g parallel to grain at upper beam contact area is changed. Lower beam width e is fixed. With a fixed e , the notch width j of the lower beam is also changed simultaneously because of the constraint condition $j + 2g = e$ (Fig. 12a).

Case 2 Length g parallel to grain at upper beam contact area is changed. The notch width j of the lower beam is fixed in this condition. Consequently, the width e of the lower beam is also changed simultaneously because of the constraint condition $j + 2g = e$ (Fig. 12b).

Case 3 Length h parallel to notch at lower beam is changed. Width a of upper beam is also changed simultaneously because of the constraint condition $a = h$ (Fig. 12c).

Case 4 Notch depth c and i of upper and lower beams is simultaneously changed because of the constraint condition $c = i$ (Fig. 12d).

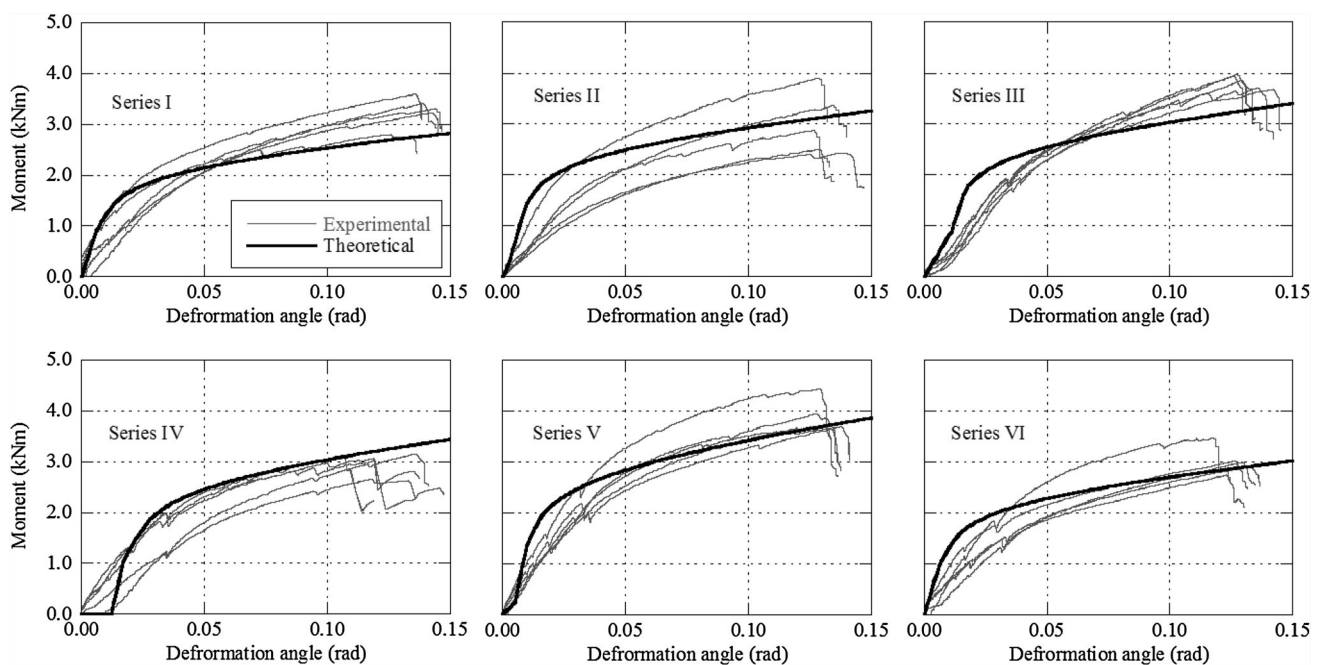


Fig. 11 Theoretical and experimental results. Series I to VI refer Table 1

Table 2 Mechanical properties of “Watari-ago” joint

Series	M_{\max} (kNm)	M_y (kNm)	K (kNm/rad)	M_u (kNm)	D_s	$M_{1/120}$ (kNm)
I	3.26	1.83	58.0	2.87	0.47	0.70
II	3.01	1.65	50.9	2.61	0.49	0.49
III	3.83	2.05	51.2	3.27	0.55	0.29
IV	2.99	1.79	47.8	2.68	0.54	0.43
V	3.89	2.23	62.0	3.50	0.51	0.66
VI	3.02	1.66	50.9	2.64	0.51	0.53

M_{\max} maximum moment, M_y moment at yield point, K rotational stiffness, M_u ultimate moment, D_s structural characteristic factor, $M_{1/120}$ moment at deformation angle 1/120 rad

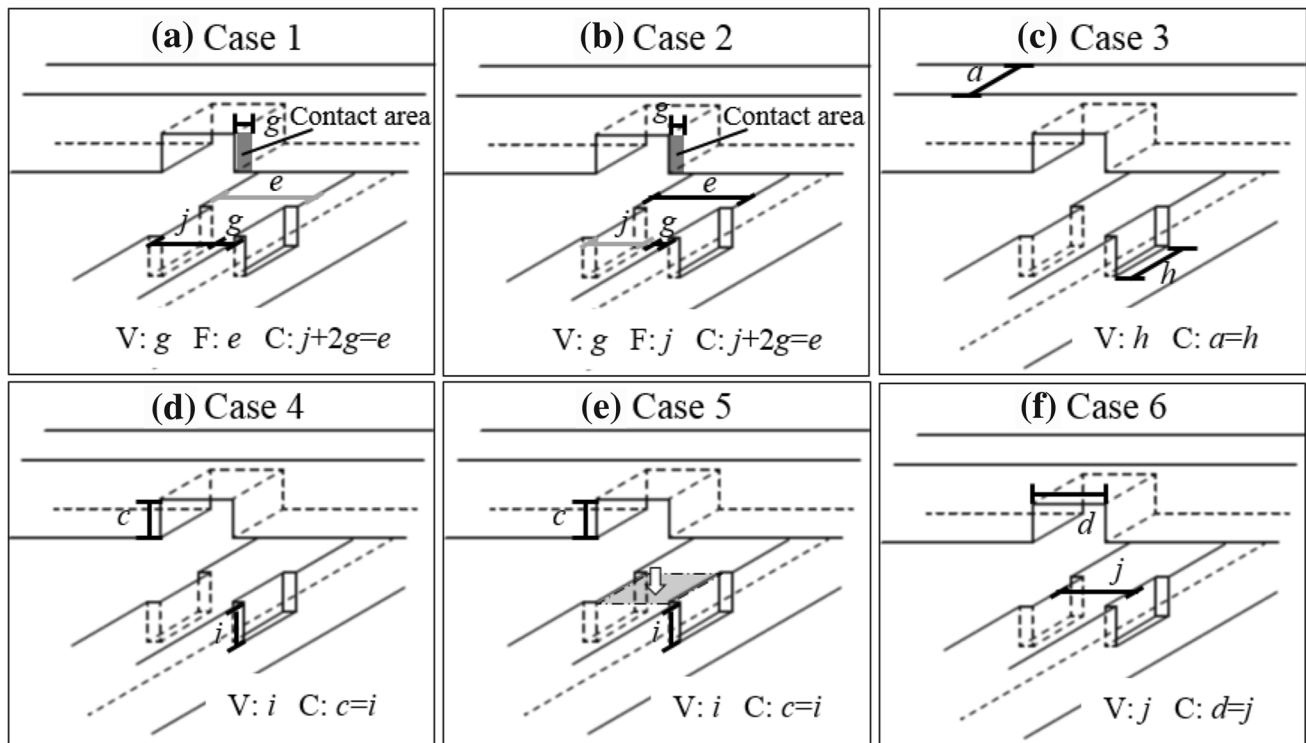


Fig. 12 Cases of change in notch size. The *black* and *gray* lines means varied and fixed, respectively. a, c, d, e, g, h and j refer Fig. 2. V, varied size parameter; F, fixed size parameter; C, constraint

Case 5 Height i of notch at lower beam is changed. Depth c of notch at upper beam is also changed because of the constraint condition $c = i$. In this case, the top surface of notch in lower beam (gray part) is moved downward. The shape of notch in lower beam become like Type B after the change of i (Fig. 12e).

Case 6 Width, j , of notch at lower beam is changed. Length d of notch at upper beam parallel to grain is also changed simultaneously because of the constraint condition $d = j$ (Fig. 12f).

Figure 13 shows the change in moment resistance with changing parameters a, b, c, \dots, j according to the above cases. The vertical axis depicts the change in moment due

condition due to geometrical relationships. In case 5, the top surface of notch in lower beam (gray part) is moved downward

to the change in dimension size. The moment of series I at deformation angle 0.1 rad is used as a standard. The horizontal axis shows the change in sizes according to the cases in Fig. 12. The sizes of series I are used as the basis of comparison. Figure 13 highlights the relationships between size changes and increase (or decrease) of moment resistance. From the graph, case 6 shows great effect on moment resistance. When j is changed to 150 % according to case 6, the change in moment is greater than 100 %. Cases 3 and 4 changes more strongly affect moment resistance than case 6. The change in moment almost reaches 50 % for size changes of 50 %. Size changes occurs the enlargement or reduction of cross section of the members. Therefore, large size changes such as 100 % are

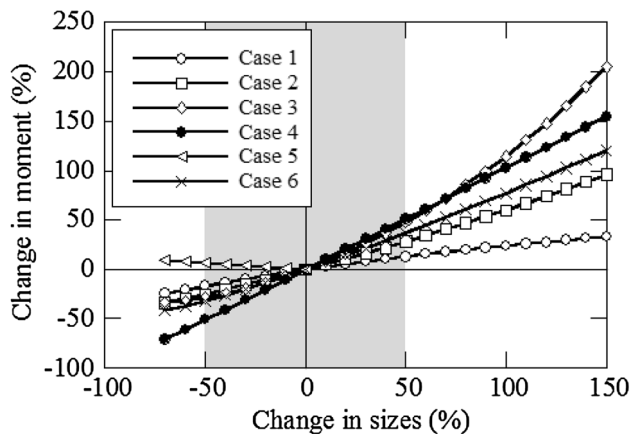


Fig. 13 Changes in moments caused by changes in notch size. Cases 1–6 refer Fig. 12

unfeasible. The authors thus propose the limit of change to the horizontal axis as -50 to 50 % (gray part in Fig. 13). Under this limit, it becomes clear that cases 3, 4, and 6 are all effective.

Conclusions

This paper described about the mechanical behavior of “Watari-ago” joints experimentally and theoretically. The experimental results showed that “Watari-ago” joints have high ductility. Their moment resistances are different depending upon the shape of the notch and the beam cross sections. For example, some specimens with large beam width showed larger maximum moment. It is also clear that the existence of gaps at the contact area causes decreased moment resistance especially during initial loading. Another significant aspect of this paper was to derive the moment resistance of “Watari-ago” joints theoretically based on wooden embedment theory. The theoretical results reflect accurately the experimental results. It is noted that the little moment resistance seen at initial loading can be expressed by considering the gaps in contact areas. Finally, the authors indicated the size parameters effective for altering the mechanical behavior of the “Watari-ago” joint by using our theoretical simulation. The results of the simulation show that optimization of beam width and notch depth increase of 50 % in terms of the joint’s moment resistance.

References

- Guan ZW, Rodd P (2001) DVW-local reinforcement for timber joints. *J Struct Eng* 127:894–900
- Leijten AJM, Ruxton S, Prion H, Lam F (2006) Reversed-cyclic behavior of a novel heavy timber tube connection. *J Struct Eng* 132:1314–1319
- Blaß HJ, Schädle P (2011) Ductility aspects of reinforced and non-reinforced timber joints. *Eng Struct* 33:3018–3026
- Shiratori T, Leijten AJM, Komatsu K (2011) Optimisation of pre/post-stressed embedment-type timber joint. *Struct Buil* 164:91–104
- Guan ZW, Kitamori A, Komatsu K (2008) Experimental study and finite element modelling of Japanese “Nuki” joints—part one: initial stress states subjected to different wedge configurations. *Eng Struct* 30:2032–2040
- Guan ZW, Kitamori A, Komatsu K (2008) Experimental study and finite element modelling of Japanese “Nuki” joints—part two: racking resistance subjected to different wedge configurations. *Eng Struct* 30:2041–2049
- King WS, Richard YJY, Alex YYN (1996) Joint characteristics of traditional Chinese wooden frames. *Eng Struct* 18:635–644
- Chang WS, Hsu MF, Komatsu K (2006) Rotational performance of traditional Nuki joints with gap I: theory and verification. *J Wood Sci* 52:58–62
- Chang WS, Hsu MF (2007) Rotational performance of traditional Nuki joints with gap II: the behavior of butted Nuki joint and its comparison with continuous Nuki joint. *J Wood Sci* 53:401–407
- Pang SJ, Oh JK, Park CY, Lee JJ (2011) Influence of crossing-beam shoulder and wood species on moment-carrying capacity in a Korean traditional dovetail joint. *J Wood Sci* 57:195–202
- Pang SJ, Oh JK, Park CY, Lee JJ (2011) Moment-carrying capacity of dovetailed mortise and tenon joints with or without beam shoulder. *J Struct Eng* 137:785–789
- Pang SJ, Oh JK, Lee JJ (2011) Alternative experimental method to evaluate moment-carrying capacity of traditional wood-to-wood joint with small scale experiment. *Holzforschung* 67:93–97
- Sadanari M (2011) Strength property of bending stress at the traditional Watariago joint (in Japanese). In: Proceedings of AIJ 2011, Tokyo, DVD 22165
- Inayama M (1993) Study on compression perpendicular to the grain in wood Part 4: analytic functions for the relation between compression load and elastic deformation perpendicular to the grain in wood (in Japanese). In: Proceedings of AIJ 1993, Tokyo, pp 907–908
- Madsen B, Hooley RF, Hall CP (1982) A design method for bearing stresses in wood. *Can J Civ Eng* 9:338–349
- Inayama M (1991) Wooden embedment theory and its application (in Japanese). Dissertation, The University of Tokyo, Tokyo, Japan
- Japan housing and wood technology center (2008) Allowable stress design for wooden framework method (in Japanese). Japan Housing and Wood Technology Center, Tokyo
- JIS Z 2101 (2009) Method of test for woods (in Japanese). Japanese Standard Association, Japan, pp 17–19, 21–22
- Architectural institute of Japan (1973) Standard for structural design of timber structures (in Japanese). Maruzen Co., Tokyo